Int j simul model 24 (2025) 2, 191-202
Original scientific paper

AERODYNAMIC AND STRUCTURAL ANALYSIS OF A SOLAR PANEL

Yemenici, O. & Oruc, E.
Department of Mechanical Engineering, University of Uludag Bursa, TR-16059 Bursa, Turkey
E-Mail: oseckin@uludag.edu.tr, emre.oruc16@gmail.com

Abstract
In this study, wind loads on a ground-mounted solar panel was investigated numerically at different ground clearances and azimuth angles, and the results were compared with the experimental data. A 1:20 scaled solar panel model with 35° panel inclinations was designed for a chord Reynolds number of 6.4×10^4. The studies were performed for the azimuth angles between 0°–180° in 30° increments and ground clearances of 0 to 0.06 m. In the numerical analyses, Computational Fluid Dynamics was calculated with 3 different turbulence models. The results showed that higher ground clearances caused stronger vortex shedding fluctuations, higher velocity zones, and shedding frequencies, and shorter vortex scales behind the panel. The critical wind directions were determined as 30° and 150° in terms of overturning moments, while the maximum value of both the lift and drag coefficient were obtained at 180° azimuth angle. In addition, a hurricane scenario with a wind velocity of 33 m/s was created on a 1:1 scaled model and fluid-structure interaction simulation was performed. The numerical results of the aerodynamic loads were in a good agreement with the experimental results.
(Received in October 2024, accepted in March 2025. This paper was with the authors 3 weeks for 2 revisions.)

Key Words: Wind Loads, Solar Panel, Turbulence Models, Computational Fluid Dynamics (CFD), Fluid-Structure Interaction (FSI)

1. INTRODUCTION

In recent years, storms and hurricanes caused by climate change exert a detrimental impact on daily life, resulting in substantial material damage and even loss of life. In 2022 alone, storms and floods in the U.S. inflicted nearly 7 billion dollars in damage, and this sum continues to increase (NOAA). Since solar photovoltaic panels, which require high installation costs, are directly susceptible to natural disasters, the strength calculations of these structures must be made meticulously. Solar energy systems produce energy using photovoltaic panels which are used on large solar panel fields and roofs. Since the panels are damaged especially under wind load, wind load calculations should be done well before installation. Therefore, there have been several investigations on the wind loads of solar panels. For instance, Jubayer and Hangan [1] investigated a photovoltaic panel installed in an open land setting, utilizing the atmospheric boundary layer approach, both numerically and experimentally. A numerical study was carried out to predict the wind loads on solar panels for different turbulence intensities ranging from 0.1 to 0.3 and wind speeds ranging from 35 to 75 m/s by Choi et al. [2]. 1:20 scaled solar panel with a 20° tilt angle were experimentally tested at different configurations by Ginger et al. [3] Shademan et al. [4] conducted 3-D Reynolds-Averaged Navier-Stokes (RANS) simulations to evaluate the flow structure on ground-mounted solar panels under various flow configurations. Güemes et al. [5] compared experimental and numerical techniques to evaluate the accuracy of RANS models in predicting wind loads on solar panels. Wang et al. [6] investigated experimentally the wind load on building-mounted solar panel systems under the effects of building side and aspect ratio and parapet height. Li et al. [7] investigated the wind load on in-line flat roof-mounted solar panels and determined the effects of array spacing, the inclination angle and parapet height. Mammar et al. [8] studied on the effect of column height on the stationary and unsteady wind loads on heliostats. An experimental study performed to determine wind loads on 1:20 scaled solar panels installed on the roofs of low-rise buildings at

different distance between modules and mounting height by Stenabaugh et al. [9]. Browne et al. [10] presented a short method to determine the wind loads on multi-row ground mounted solar panel models compliant with ASCE 7 (The American Society of Civil Engineers) standards and the resulting dynamic resonance effects with reference to wind tunnel experiments. Barbón et al. [11] examined in-line ground-mounted solar panel systems and presented a method for estimating the optimum locations for such systems. Young et al. [12] investigated aeroelastic fluctuations due to strong winds on solar tracking solar panel systems. Aly and Whipple [13] simulated a hurricane with two different configurations for ground-mounted panels under the effect of the tilt angle, ground clearance and bracket lengths. Leitch et al. [14] investigated the net wind loads on solar panels that were mounted parallel to pitched roofs and on the underlying roof surface. Yemenici and Aksoy [15] performed an experimental and numerical study on wind effects of a ground-mounted solar panel at different panel inclinations and azimuth angles. CFD method enables the detection of potential errors before the production process begins. Danesho et al. [16] demonstrated the effectiveness of this method by predicting faults in their models.

In the literature, the studies of aerodynamic characteristics of solar panel systems have mainly focused on roof-mounted and building-mounted systems. Although in recent years, investigations about ground-mounted systems and solar energy farms have become more essential due to increasing energy demand, most of these were either experimental or numerical. To fill this gap, the wind loads on a ground-mounted solar panel were investigated under the effect of the ground clearances and azimuth angles, both experimentally and numerically. In addition, the stresses on the panel were calculated using the FSI method. More cost-effective systems were designed in a shorter time with numerical analyses using RSM, k-ε and k-ω SST (Shear Stress Transport) turbulence models and these analyses were compared among themselves and with experimental results. Moreover, the use of two different ground clearances in the research provided a design method for solar power plants in different terrain conditions and offshore installation.

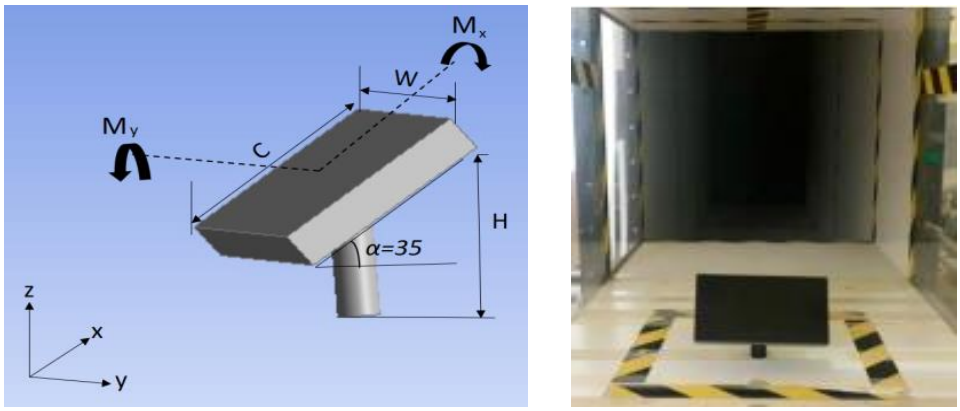
2. METHODOLOGY

In this section, the experimental setup, the numerical methods, the flow conditions, and the measuring instruments are examined in detail. The dimensions of the flow field, boundary conditions, mesh structure, mesh independence study, conservation equations, and validation study are also presented. In addition, the FSI method, which allows the numerical calculation of stresses due to wind loads, is also detailed.

2.1 Experimental set-up

Figs. 1 a and 1 b show the geometry, moment coordinate system and position of the 1:20 scale solar panel model in the wind tunnel. As stated in the literature by Yemenici and Aksoy [15] and Aly and Whipple [13], the front row panels of solar panel arrays are subjected to maximum aerodynamic loads. Therefore, a single ground-mounted solar panel model is designed and predictions are made for the other panels based on this model. The panel with a width of 0.2 m, a beam of 0.1 m and a thickness of 0.02 m is fixed to a support column with a diameter of 0.02 m by bolt-nut. The thickness of the panel was kept to a minimum to allow the pressure tubes to fit, and the support column made of stainless steel was placed on the turntable. Experimental and numerical analyses were performed using a panel inclination angle of 35°. The ground clearance was 0 and 0.06 m and the azimuth angles were 0°, 30°, 60°, 90°, 120°, 150° and 180°. The panel was located 0.05 m from the entrance of the wind tunnel test section. For simultaneous pressure measurements, a total of 50 pressure taps were opened on the top and bottom surfaces of the panel, 25 taps on each surface. The taps were spaced at regular

intervals across the width of the panel and the floor opening and connected to the scanner system via pressure pipes. The Re_C was calculated as 6.4×10^4, and the reference wind speed was chosen as 10 m/s for all measurements.



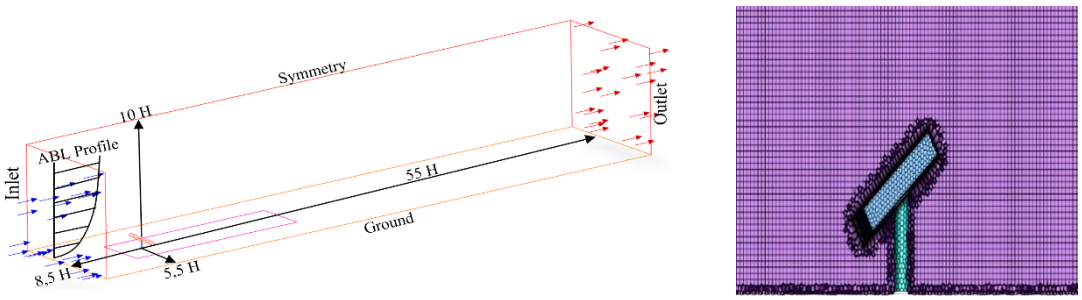
a) b)

Figure 1: a) Geometry and moment coordinate system of the model, b) 1:20 scaled model in the wind tunnel.

In order to obtain better understandable and more accurate experimental results, the Moffat [17] uncertainty estimation method was applied to the calculated and measured quantities. The maximum uncertainty of the velocity measurements was obtained as ±2.12 %, while those of pressure measurements value was 1.05 %. The overall uncertainty in the mean drag, pressure, lift, and moment coefficients were ±1.36 %, ±1.18 %, ±1.38 %, and ±1.38 %, respectively. The uncertainty of the Reynolds number was also approximately ±2.30 %.

2.2 Numerical methods

The solar panel was modelled using ANSYS 2020 R2 design and analysis software. The test section, solar panel dimensions, cylindrical support column, solar panel location, and the input and output parameters in the numerical simulations were designed similarly with the experimental studies. Due to the atmospheric conditions, the computational domain was created with the COST guide suggested by Franke et al. [18]. The computational domain, boundary conditions and mesh structure are shown in Figs. 2 a and 2 b. The dimensions of the domain were determined as 58.5 *H* length, 10 *H* height and 11 *H* width in order to minimize the wall effects. The maximum blockage rate was calculated approximately 1.7 %. Atmospheric boundary conditions were determined based on the flow conditions of the wind tunnel, and the *TI* was chosen 20 % at a reference inlet velocity of 10 m/s. No-slip wall condition was applied at the domain walls, panel surface and support column. The zero-pressure gradient was used at the outlet domain. Polyhedral-hexahedral mesh structures were created with the FLUENT 2020 R2 meshing program. In general, fine mesh structures were formed in domains with more gradient changes, while coarser mesh structures were formed in the other areas. Thus, the minimum CPU usage and analysis times were obtained. The mesh independence study was performed for the estimation of discretization error, as stated by Celik et al. [19]. The grid sensitivity analyses were carried out with the number of 2213117, 4337759 and 10269099 elements for the panel inclination of 35° and the azimuth angle of 0°. The *GCI* values of velocities were calculated as 0.79 % and 1.4 % for the medium and finest mesh structures, while those of value based on the mean surface pressures were 7.89 % and 9.28 %, respectively. As a result, it was determined that the number of 4337759 elements was sufficient in terms of accuracy and the analyses were carried out with medium grid.



a) b)

Figure 2: a) Computational domain and boundary conditions, b) mesh structure.

In the numerical analyses, simulations were performed with the *k-ε*, *k-ω* SST and RSM turbulence models, which were detailed in this section. RANS models provide numerical solutions for simple and complex problems for laminar or turbulent flows in fluid mechanics and dynamics. RANS methods are based on the Reynolds decomposition of the Navier-Stokes equations, and turbulent flow is defined as a random variation around a mean value. The time-averaged mass-conservation and the Reynolds-averaged Navier-Stokes equations described as:

$$\frac{\partial U_i}{\partial x_i} = 0 \tag{1}$$

$$\rho \frac{\partial U_i}{\partial t} + \rho U_j \frac{\partial U_i}{\partial x_j} = -\frac{\partial P}{\partial x_i} + \frac{\partial}{\partial x_j}(2\mu S_{ji} - \rho\overline{u_j' u_i'}) \tag{2}$$

where ρ is fluid density, P is static pressure, and u_i and u_j are fluid velocities in tensor form. The Reynolds stress term $\rho\overline{u_j' u_i'}$ was defined as $\rho\overline{u_j' u_i'} = \rho\tau_{ij}$ and $S_{i,j}$ were given with Eq. (3).

$$S_{i,j} = \frac{1}{2}\left(\frac{\partial u_i}{\partial x_j} + \frac{\partial u_j}{\partial x_i}\right) \tag{3}$$

The *k-ω* SST model uses two transport equations, one for the turbulent kinetic energy (k) and one for the specific dissipation rate of the turbulent kinetic energy (ω). The specific dissipation rate, which is defined as the rate of dissipation of turbulent kinetic energy per unit mass, is used to compute the turbulent viscosity in the model. It provides more accurate solutions for both separated and free shear flows, as stated by Czyz and Karpinski [20]. The turbulence viscosity, turbulent kinetic energy, and specific dispersion ratio equations was given as:

$$\nu_t = a_1 \frac{k}{max(a_1\omega, b_1 F_{23} S)} \tag{4}$$

$$\frac{D}{Dt}(\rho k) = \nabla \cdot (\rho D_k \nabla k) + \rho G - \frac{2}{3}\rho k(\nabla \cdot u) - \rho\beta^* \omega k + S_k \tag{5}$$

$$\frac{D}{Dt}(\rho\omega) = \nabla.(\rho D_\omega \nabla\omega) + \frac{\rho\gamma G}{\nu} - \frac{2}{3}\rho\gamma\omega(\nabla.u) - \rho\beta\omega 2 - \rho(F1-1)CD_{k\omega} + S_\omega \tag{6}$$

In the simulations, mean drag and lift coefficients values of the panel were obtained for seven different azimuth angles and two different ground clearances. The numerical C_D and C_L values were evaluated using the RSM, *k-ε* and *k-ω* SST turbulence models. The results obtained for each turbulence model were compared with the experimental data in Fig. 3. It was seen that the results of RSM, *k-ε* and *k-ω* SST turbulence models were similar to the experimental results with error rates of 1.2 %, 4.3 % and 1.9 % for C_D, 3.1 %, 4.9 % and 3.9 % for C_L at H6 height, respectively. Similarly, those of values at the H0 model were found as 2.7 %, 6.8 % and 3.2 % for C_D, 12.7 %, 15.6 % and 13.4 % for C_L, respectively. The error difference between the RSM model and the *k-ω* SST model was smaller than 1 % on average. For this reason, the *k-ω* SST turbulence model was chosen in the analysis to better observe the flows around the panel and to reduce CPU and time costs.

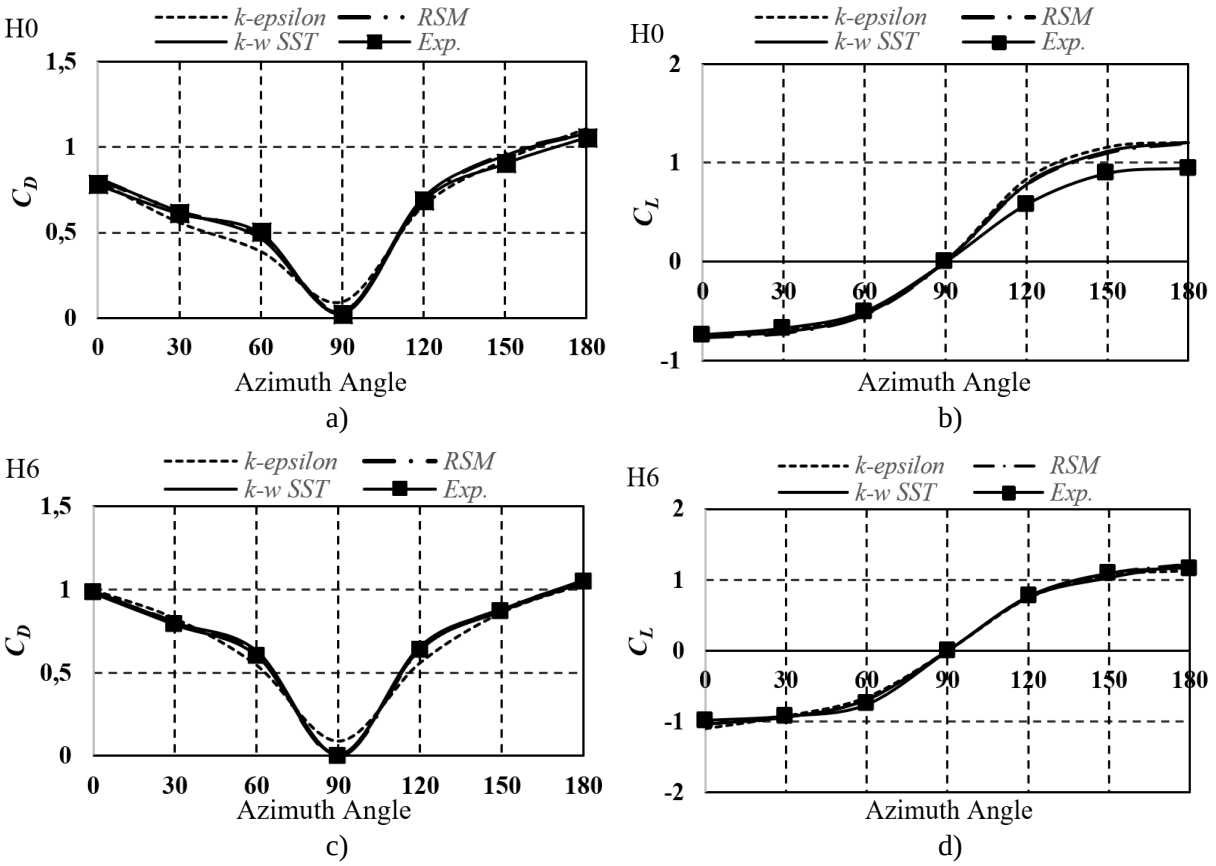


Figure 3: C_L and C_D plots of each turbulence models compared with experimental data.

The average CPU time per iteration for each turbulence model and azimuth angle is given in Fig. 4. The RSM model consumed a higher CPU time compared to the other two models, which results in higher costs. Although the difference between the RSM and *k-ω* SST model results were very small, the *k-ω* SST model was the most optimal turbulence model in terms of CPU costs and time. Therefore, the *k-ω* SST model was used as turbulence model in this study.

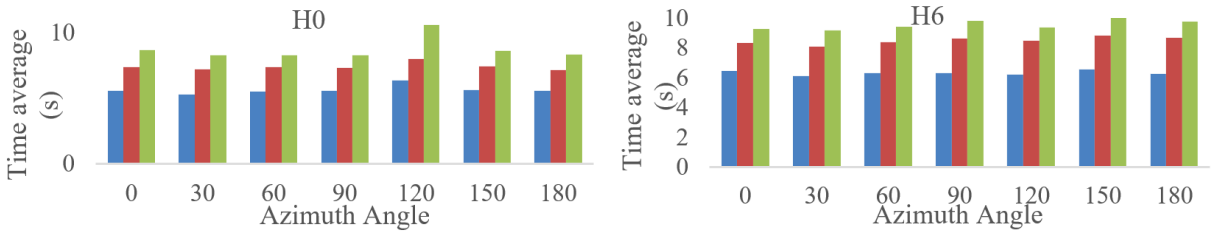


Figure 4: The average CPU time per iteration for each turbulence model and azimuth angle.

Finite Volume Method and the QUICK scheme was used in the analysis to discretize the governing equations and convective terms, respectively. For pressure interpolation, the STANDARD scheme based on the mean values of the flow variables was performed. The SIMPLE algorithm was applied to obtain the pressure-velocity matching. Simulations were considered to converge when insignificant changes in the drag and lift forces of the panels were observed. Seven different cases were simulated for azimuth angle effect and two different cases for ground clearance. In addition, the numerical results were validated by comparing with experimental results as applied by Wan et al. [21].

In many CFD-based aerodynamic problems, it is assumed that the forces exerted by the fluid on the bounding solid surfaces do not significantly change their geometry. In such cases, the interaction of the fluid with the solid surfaces can be studied and the forces exerted on the

solid surfaces can be calculated once the characteristics of the fluid motion are determined, as stated by Antoci et al. [22]. If the characteristic time scales of the motion of the fluid and the solid surface are similar, it is necessary to match the dynamics of the two domain. The fluid-structure interaction (FSI) problems can be solved using a simultaneous solution or a split solution from Rugonyi and Bathe [23].

The aerodynamic loads on the 1/10 scaled solar panel model were investigated experimentally and the values were compared with numerical data. Then, all numerical parameters are kept constant and analysed in a hurricane scenario with a real-size model. According to the World Meteorological Organization, wind velocity of 74 mph (33 m/s) or higher are classified as hurricanes, typhoons or tropical cyclones depending on where the storm is located. For this reason, the wind velocity was determined as 33 m/s in the numerical study for the real-size model. The real-size model was reanalysed at a wind velocity of 33 m/s using data from an experimentally validated CFD study. The mesh structure and boundary conditions of the structural model were determined separately from the CFD study. Hexadominant mesh structure was used as the mesh element. Structural steel, the most used material in solar panel farms, was selected as the outer protection and support material. The model was set to be fixed to the ground from the support column. In order to simplify the model, other small-scale auxiliary equipment on the solar panel was not considered. The pressure data of the CFD were interpolated on the panel surfaces. The mesh structure of the panel design is shown in Fig. 5.

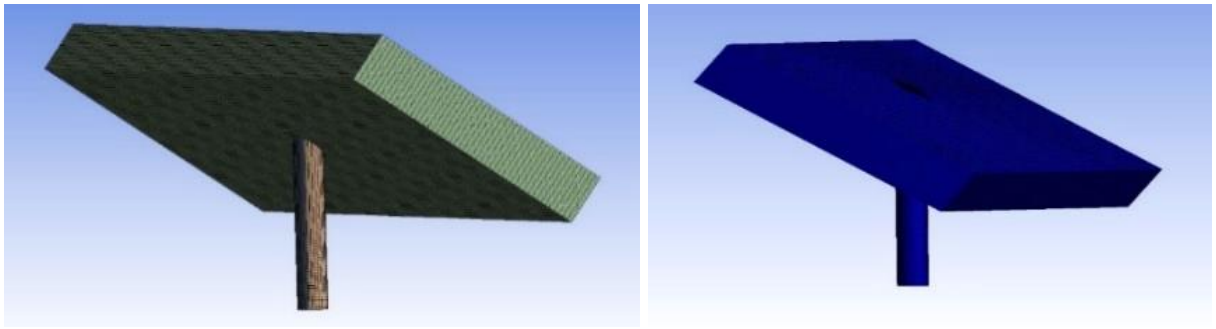


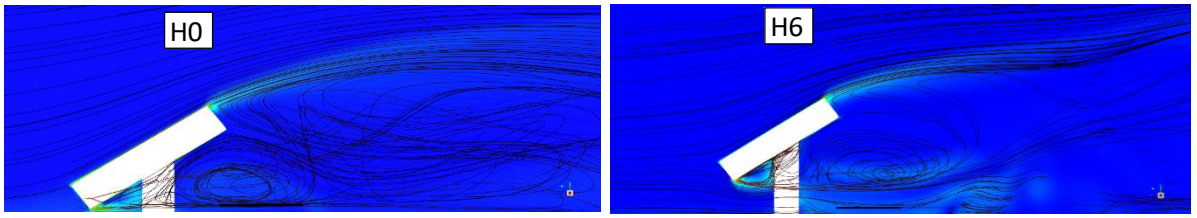
Figure 5: Mesh structure of the panel design.

3. RESULT AND DISCUSSION

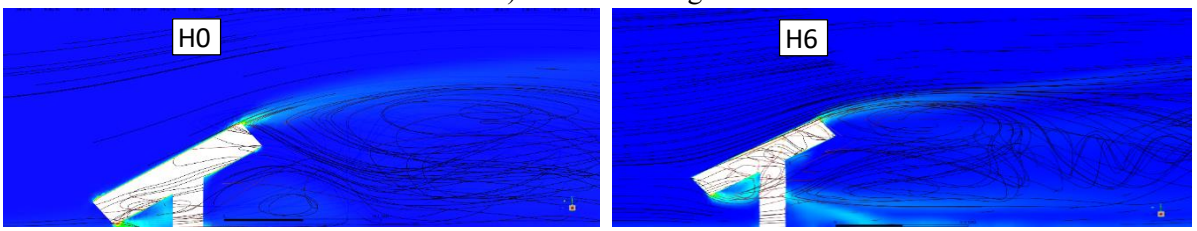
In this section, the flow field, the pressure distributions and the aerodynamic loads around the panel are presented at different azimuth angles and ground clearance. In addition, the stresses on the solar panel due to wind loads were calculated using FSI method. The results of total deformation and equivalent Von Mises stresses are also discussed.

The flow streamlines with the vorticity magnitudes of the panel with H0 and H6 height for the azimuth angles in increments of 30° from 0° to 180° in Figs. 6 a to g, respectively. For the model with H6 height and 0° azimuth angle, the high intensity and small-scale vortex were observed at the leading and escape edge where the wind hits and leaves the panel, respectively. Also, the air under the panel created larger vortices around the support column. The flow separated downstream caused a smaller vortex between the leading edge and the support column on the bottom surface of the panel due to the wall effects. For the 30° azimuth angle, the vortex around the support column were larger in diameter and smaller in intensity than those of obtained at 0°. The vortex formation was determined at the escape edge. The small-scale local vortices were obtained on the panel edge for the azimuth angles of 60° and 120°, in contrast to 0° and 30° angles. The flow patterns on the lower and upper surfaces of the panel were similar for 90° azimuthal angle. Since the flow mostly affected the bottom surface of the panel, the flow of the leading and escape edge created vortices of two different diameters and

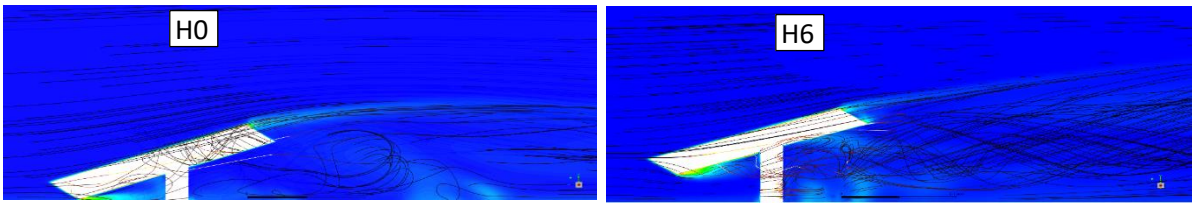
densities for the 150° azimuthal angle. For the azimuthal angle of 180°, a large-scale vortex occurred on the upper surface of the panel from the leading edge to the escape edge, and a small-scale high-intensity vortex obtained after the leading edge. The vortices diameters of this azimuthal angle were larger than those of the other angles.



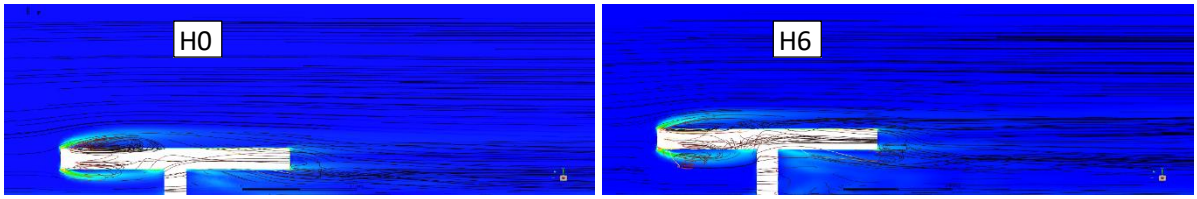
a) 0° azimuth angle



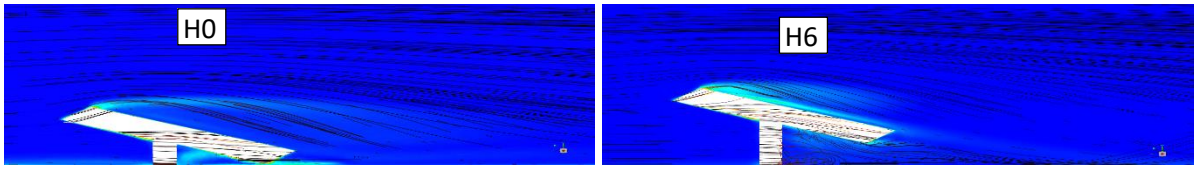
b) 30° azimuth angle



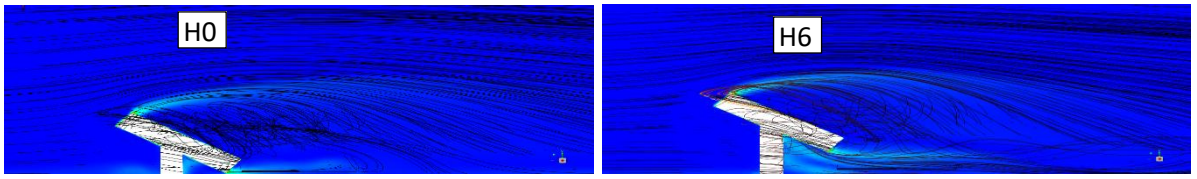
c) 60° azimuth angle



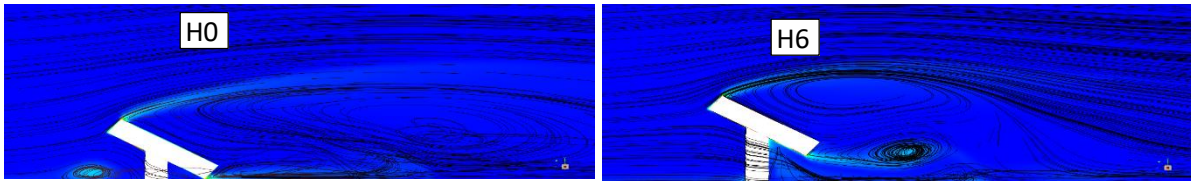
d) 90° azimuth angle



e) 120° azimuth angle



f) 150° azimuth angle

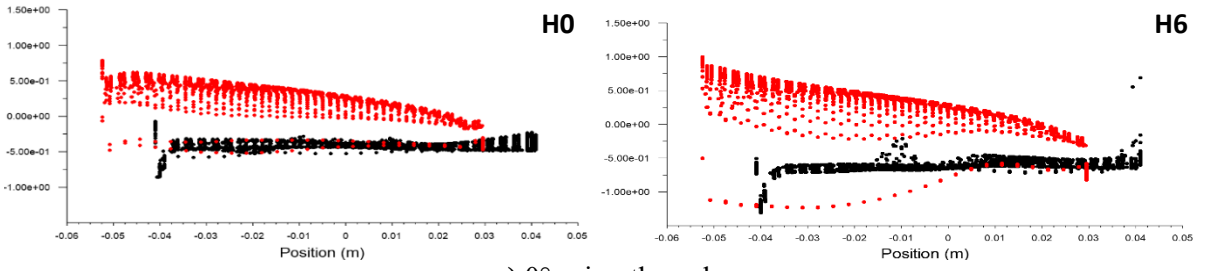


g) 180° azimuth angle

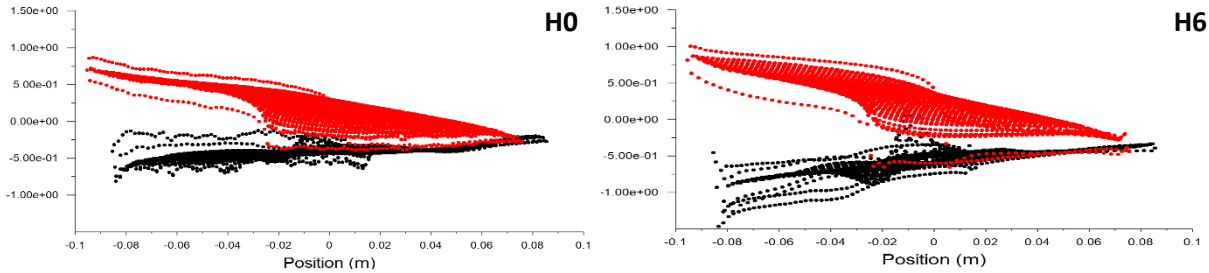
Figure 6: The contours of vorticity magnitudes of panel with H0 and H6 height for the azimuth angles of a) 0°, b) 30°, c) 60°, d) 90°, e) 120°, f) 150° and g) 180°.

For both ground clearances, the stagnation points occurred at the leading edge of the panel, and the wind velocity accelerated from the leading to trailing edge. The vortex scales behind the panel with the ground clearance of H0 were larger than those of H6 height. The reattachment occurred farther away from the panel, due to zero flow behind the panel with H0 height. The vortex regions of the panel with H6 ground clearance lost their effects at a shorter distance.

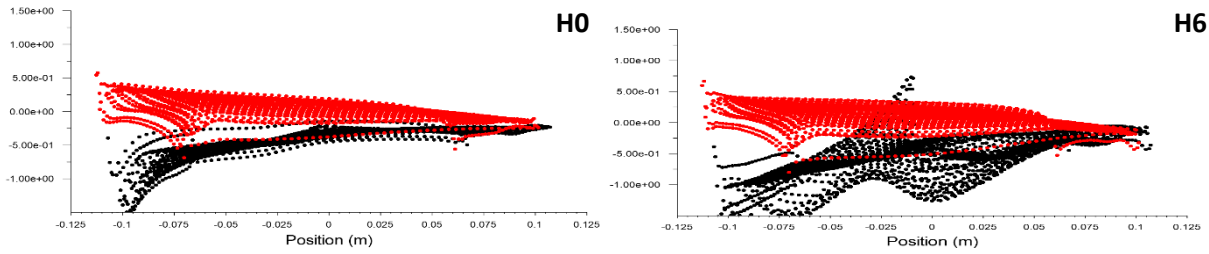
The pressure coefficient distributions of panel with H0 and H6 height for the azimuth angles from 0° to 180° are shown in Figs. 7 a to g, respectively. For both ground clearances, the C_P values of the leading edge where the wind first contacted the panel were higher than the values of trailing edge where the wind leaves the panel. The C_P values decreased from the leading to the trailing edge of the panel, and the values also reduced due to the vortices behind the panel. The support column caused high C_P values because of the flow resistance. The pressure coefficient distributions were similar for symmetric angles of 0° and 180°, 30° and 150°, and 60° and 120° azimuth angles. For the azimuth angle of 90°, the C_P values showed almost equal distribution for both the upper and lower surfaces of the panel. The maximum C_P values occurred at the azimuth angle of 180° that the panel was perpendicular to the flow direction, as stated by Shademan et al. [24].



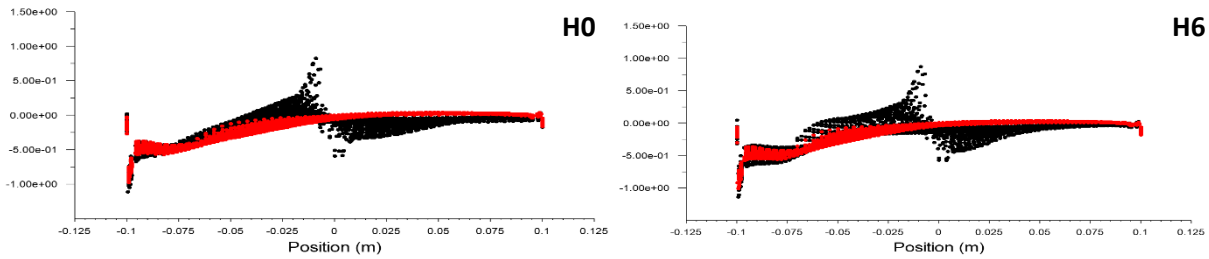
a) 0° azimuth angle



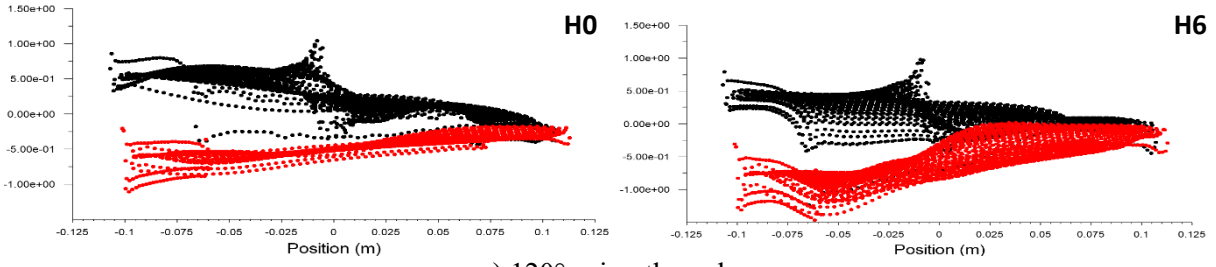
b) 30° azimuth angle



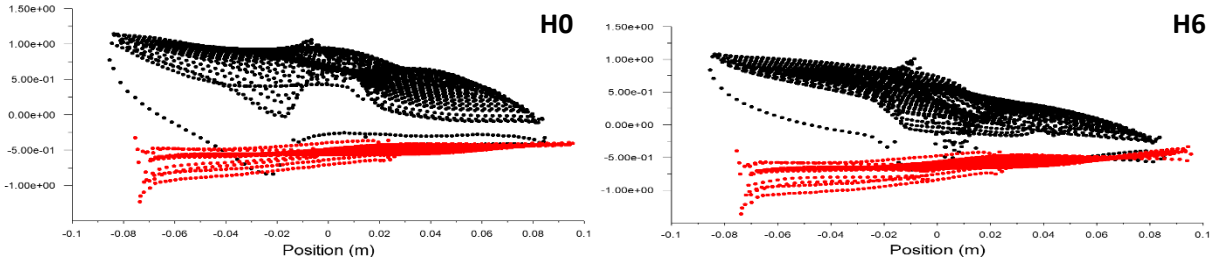
c) 60° azimuth angle



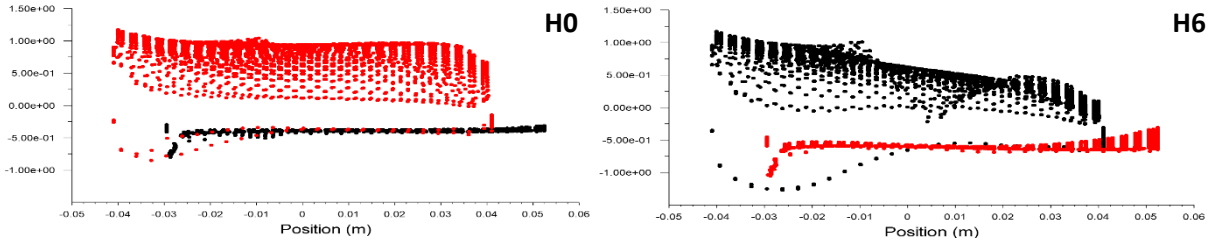
d) 90° azimuth angle



e) 120° azimuth angle



f) 150° azimuth angle



g) 180° azimuth angle

Figure 7: The pressure coefficient distributions of panel with H0 and H6 height for the azimuth angles of a) 0°, b) 30°, c) 60°, d) 90°, e) 120°, f) 150° and g) 180°.

The results showed that the azimuth angles and ground clearance affected the C_P coefficients. For the same azimuth angles, the C_P values of the panel with the H6 height were higher than those of H0 values. The average pressure difference between the windward and leeward surface of the panel increased with the ground clearance, resulting in higher wind loads and stronger eddy shedding, as reported by Mammar et al. [8]. In addition, the flow passed through the gap between the ground and the panel more easily due to lower friction effects, less blockage, and less interference from the ground. The flow structures at both the leading and trailing edges of the panel surface was affected by changes in ground clearance. The lower regions close to the leading edge were more sensitive to wind loads and had the maximum pressure difference compared to the upper edge, as stated by Abiola-Ogedengbe [25].

In Fig. 8 at different azimuth angles, the experimental and numerical average drag coefficient values of the solar panel with H0 and H6 ground clearances reached a maximum at 0° azimuth angle and decreased to a minimum at 90°. For the H0 panel, the C_D value was found to be 0.77 at 0° azimuth angle and 0.97 for H6. The C_D values increased as the ground clearance of the panel increased. Experimental and numerical C_D values were similar for both panels with a mean error of 3.4 % and 2.05 %, respectively. The coefficient of lift was maximum at 180° azimuth angle and minimum at 90°. In panel H6, the C_L value was 1.16 at 180° azimuth angle. The experimental and numerical C_L values gave consistent results with error rates of 3.9 % and 13.4 %. It was observed that the aerodynamic loads increased as the ground clearance increased.

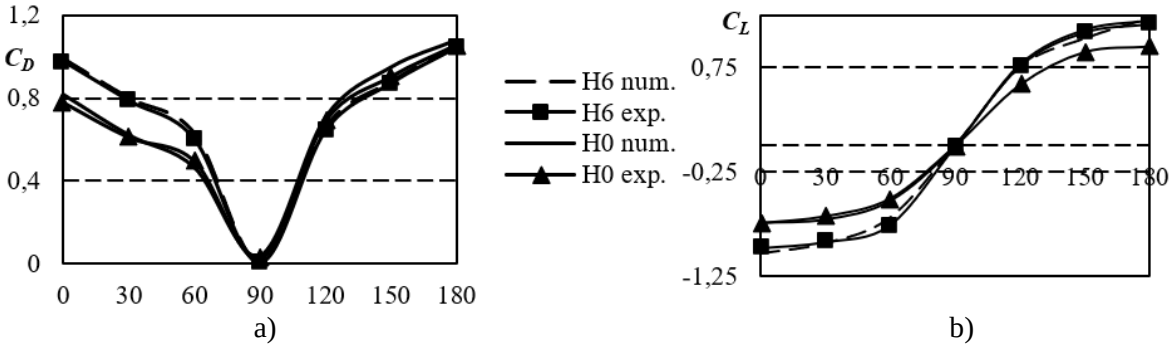


Figure 8: The numerical and experimental mean; a) drag coefficients, b) lift coefficients.

The average overturning moment coefficients of the solar panel in the experimental and numerical x (M_x) and y (M_y) axes for different ground clearances and azimuth angles were analysed and the results are given in Fig. 9. The maximum positive and negative M_x values for models H6 and H0 were measured as 0.57 and -0.47 at azimuth angles of 30° and 150°, respectively. The average error between M_x values is 17.9 % for H0 and 16.4 % for H6. In the M_y axis, the maximum positive and negative values were observed at azimuth angles of 0° and 180°, with error rates of 10.1 % for H0 and 9.8 % for H6, showing agreement between experimental and numerical results.

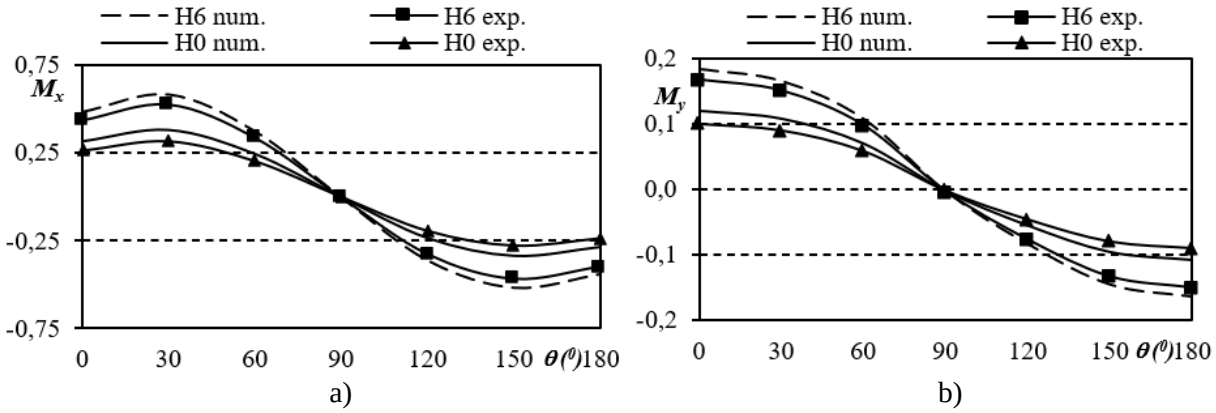


Figure 9: The experimental and numerical a) x-axis (M_x) and b) y-axis (M_y) mean overturning moment coefficients.

Following the experimental and numerically studies, an FSI study was conducted for the 1:1 scaled panel model. A hurricane scenario with a wind speed of 33 m/s was created for the model with a height of H6 and an azimuth angle of 180°, which the wind load was most effective. Fig. 10 shows the total deformation and equivalent Von Mises stresses on the solar panel model. Aerodynamic loads and structural stresses on the panel and support column were analysed. The stresses were found to be mostly around the connection points and the maximum stress was found to be 145.86 MPa in this region. In addition, the highest value of the total deformation was 0.5 mm.

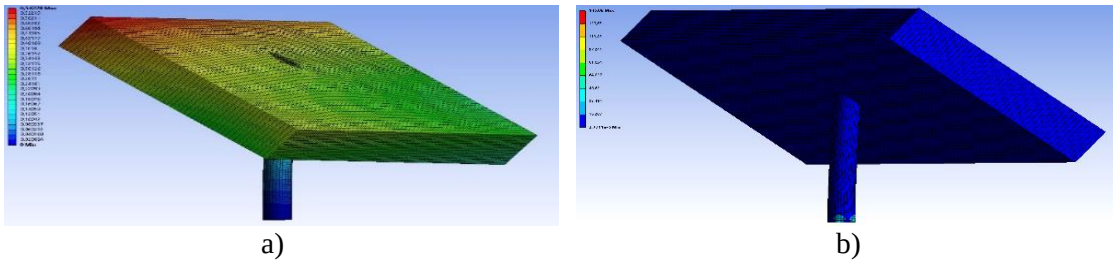


Figure 10: a) Total deformation, b) Von Mises stresses on the solar panel.

4. CONCLUSION

Numerical and experimental research was conducted on the flow over the solar panel model with the ground clearance of H0 and H6 for the azimuth angle of 0°, 30°, 60°, 90°, 120°, 150° and 180°.

It was determined that the ground clearance of the panels and the azimuth angles significantly changed the flow structure around the panels, accordingly lift, drag and overturning moments. The high-intensity and small-scale vortex effects were observed on the leading and leeward edge of the panel, while larger-scale vortices formed around the support column. The vortex scales decreased, as the azimuth angle increased from 0° to 90°. For 180° azimuth angle, a large-scale vortex was obtained on the upper surface of the panel. The larger and more intense vortices occurred in the rear region of the panel with H0 ground clearance for 0° azimuth angle, compared to the panel with H6 ground clearance. The pressure coefficients of the panel with the ground clearance of H6 were higher than those of H0 for the same azimuth angles. The C_P values on the leading edge of the panel were found greater than those of the value on the trailing edge. The lower C_P values were determined on the bottom surface of the panel, while higher values were observed at the centre of the panel. The maximum values of C_D and C_L for both ground clearances occurred at 180° azimuth angle. The highest positive and negative M_x values were found to be at 30° and 150° azimuth angles, respectively, while those of M_y values were determined at 0° and 180° azimuth angles. In terms of uplift and drag, 180° was the critical azimuth angle, while 30° and 150° were critical wind directions in terms of overturning moments. The numerical results of the aerodynamic loads were in good agreement with the experimental results for all ground clearances and azimuth angles.

The study demonstrated that stress strength of the panels can be determined at different wind velocities and loads, and the one-way FSI method provides a safe design at optimum cost by determining the effects of aerodynamic loads on the structural geometry of the panels. The high stress values were obtained around the connection points and the maximum stress value of the total deformation was determined as 0.5 mm.

REFERENCES

[1] Jubayer, C. M.; Hangan, H. (2016). A numerical approach to the investigation of wind loading on an array of ground mounted solar photovoltaic (PV) panels, *Journal of Wind Engineering and Industrial Aerodynamics*, Vol. 153, 60-70, doi:10.1016/j.jweia.2016.03.009

[2] Choi, S. M.; Lee, G. R.; Park, C. D.; Cho, S. H.; Lim, B. J. (2021). Wind load on the solar panel array of a floating photovoltaic system under extreme hurricane conditions, *Sustainable Energy Technologies and Assessments*, Vol. 48, Paper 101616, 14 pages, doi:10.1016/j.seta.2021.101616

[3] Ginger, J. D.; Bodhinayake, G. G.; Ingham, S. (2019). Wind loads for designing ground-mounted solar-panel arrays, *Australian Journal of Structural Engineering*, Vol. 20, No. 3, 204-218, doi:10.1080/13287982.2019.1623001

[4] Shademan, M.; Balachandar, R.; Barron, R. M. (2014). Detached eddy simulation of flow past an isolated inclined solar panel, *Journal of Fluids and Structures*, Vol. 50, 217-230, doi:10.1016/j.jfluidstructs.2014.06.024

[5] Güemes, A.; Fajardo, P.; Raiola, M. (2021). Experimental assessment of RANS models for wind load estimation over solar-panel arrays, *Applied Sciences*, Vol. 11, No. 6, Paper 2496, 14 pages, doi:10.3390/app11062496

[6] Wang, J.; Yang, Q.; Tamura, Y. (2018). Effects of building parameters on wind loads on flat-roof-mounted solar arrays, *Journal of Wind Engineering and Industrial Aerodynamics*, Vol. 174, 210-224, doi:10.1016/j.jweia.2017.12.023

[7] Li, S.; Mao, D.; Li, S.; Wang, Q.; Yang, Q.; Chen, Y.; Zhou, S. (2022). Wind load characteristics of photovoltaic panel arrays mounted on flat roof, *Engineering Research Express*, Vol. 4, No. 1, Paper 015027, 14 pages, doi:10.1088/2631-8695/ac57fc

[8] Mammar, M.; Djouimaa, S.; Gärtner, U.; Hamidat, A. (2018). Wind loads on heliostats of various column heights: an experimental study, *Energy*, Vol. 143, 867-880, doi:10.1016/j.energy.2017.11.032

[9] Stenabaugh, S. E.; Iida, Y.; Kopp, G. A.; Karava, P. (2015). Wind loads on photovoltaic arrays mounted parallel to sloped roofs on low-rise buildings, *Journal of Wind Engineering and Industrial Aerodynamics*, Vol. 139, 16-26, doi:10.1016/j.jweia.2015.01.007

[10] Browne, M. T. L.; Taylor, Z. J.; Li, S.; Gamble, S. (2020). A wind load design method for ground-mounted multi-row solar arrays based on a compilation of wind tunnel experiments, *Journal of Wind Engineering and Industrial Aerodynamics*, Vol. 205, Paper 104294, 23 pages, doi:10.1016/j.jweia.2020.104294

[11] Barbón, A.; Bayón-Cueli, C.; Bayón, L.; Carreira-Fontao, V. (2022). A methodology for an optimal design of ground-mounted photovoltaic power plants, *Applied Energy*, Vol. 314, Paper 118881, 20 pages, doi:10.1016/j.apenergy.2022.118881

[12] Young, E.; He, X.; King, R.; Corbus, D. (2020). A fluid-structure interaction solver for investigating torsional galloping in solar-tracking photovoltaic panel arrays, *Journal of Renewable and Sustainable Energy*, Vol. 12, No. 6, Paper 063503, 9 pages, doi:10.1063/5.0023757

[13] Aly, A. M.; Whipple, J. (2021). Wind forces on ground-mounted photovoltaic solar systems: a comparative study, *Applied Solar Energy*, Vol. 57, No. 5, 444-471, doi:10.3103/S0003701X21050030

[14] Leitch, C. J.; Ginger, J. D.; Holmes, J. D. (2016). Wind loads on solar panels mounted parallel to pitched roofs, and acting on the underlying roof, *Wind and Structures*, Vol. 22, No. 3, 307-328, doi:10.12989/was.2016.22.3.307

[15] Yemenici, O.; Aksoy, M. O. (2021). An experimental and numerical study of wind effects on a ground-mounted solar panel at different panel tilt angles and wind directions, *Journal of Wind Engineering and Industrial Aerodynamics*, Vol. 213, Paper 104630, 17 pages, doi:10.1016/j.jweia.2021.104630

[16] Daneshjo, N.; Mares, A.; Malega, P.; Francova, Z. (2022). CAD model of rear-view mirror and simulation of its aerodynamics and noise, *International Journal of Simulation Modelling*, Vol. 21, No. 2, 226-236, doi:10.2507/IJSIMM21-2-598

[17] Moffat, R. J. (1988). Describing the uncertainties in experimental results, *Experimental Thermal and Fluid Science*, Vol. 1, No. 1, 3-17, doi:10.1016/0894-1777(88)90043-X

[18] Franke, J.; Hellsten, A.; Schlünzen, K. H.; Carissimo, B. (2007). Best practice guideline for the CFD simulation of flows in the urban environment – a summary, *11th Conference on Harmonisation within Atmospheric Dispersion Modelling for Regulatory Purposes*, 1-52, Cambridge

[19] Celik, I. B.; Ghia, U.; Roache, P. J.; Freitas, C. J.; Coleman, H.; Raad, P. E. (2008). Procedure for estimation and reporting of uncertainty due to discretization in CFD applications, *Journal of Fluids Engineering*, Vol. 130, No. 7, Paper 078001, 4 pages, doi:10.1115/1.2960953

[20] Czyz, Z.; Karpinski, P. (2020). Aerodynamic characteristics of the X-tail stabilizer in a hybrid unmanned aircraft, *International Journal of Simulation Modelling*, Vol. 19, No. 4, 631-642, doi:10.2507/IJSIMM19-4-534

[21] Wan, L.; Yuan, Y.; Sun, H.; Qu, J. (2023). Simulation study on drop and explosion performance of marine steam-water separator, *International Journal of Simulation Modelling*, Vol. 22, No. 3, 497-507, doi:10.2507/IJSIMM22-3-CO12

[22] Antoci, C.; Gallati, M.; Sibilla, S. (2007). Numerical simulation of fluid–structure interaction by SPH, *Computers & Structures*, Vol. 85, Nos. 11-14, 879-890, doi:10.1016/j.compstruc.2007.01.002

[23] Rugonyi, S.; Bathe, K. J. (2001). On finite element analysis of fluid flows fully coupled with structural interactions, *Computer Modeling in Engineering & Sciences*, Vol. 2, No. 2, 195-212, doi:10.3970/cmes.2001.002.195

[24] Shademan, M.; Barron, R. M.; Balachandar, R.; Hangan, H. (2014). Numerical simulation of wind loading on ground-mounted solar panels at different flow configurations, *Canadian Journal of Civil Engineering*, Vol. 41, No. 8, 728-738, doi:10.1139/cjce-2013-0537

[25] Abiola-Ogedengbe, A. (2013). *Experimental Investigation of Wind Effect on Solar Panels*, Master Thesis, The University of Western Ontario, London, Ontario